Editors' Suggestion

Broad-wave-vector spin pumping of flat-band magnons

Jinlong Wang,[1,‡] Hanchen Wang,[2,*,‡] Jilei Chen,[3,4,‡] William Legrand,[2,‡] Peng Chen,[5,‡] Lutong Sheng,[1] Jihao Xia,[5] Guibin Lan,[5] Yuelin Zhang,[1] Rundong Yuan,[1] Jing Dong,[5] Xiufeng Han,[5] Jean-Philippe Ansermet,[6] and Haiming Yu[1,3,†]

[1] *Fert Beijing Institute, MIIT Key Laboratory of Spintronics, School of Integrated Circuit Science and Engineering, Beihang University, Beijing 100191, China*

[2] *Department of Materials, ETH Zurich, Zurich 8093, Switzerland*

[3] *International Quantum Academy, Shenzhen 518055, China*

[4] *Shenzhen Institute for Quantum Science and Engineering (SIQSE), and Department of Physics, Southern University of Science and Technology (SUSTech), Shenzhen 518055, China*

[5] *Beijing National Laboratory for Condensed Matter Physics, Institute of Physics, University of Chinese Academy of Sciences, Chinese Academy of Sciences, Beijing 100190, China*

[6] *Institute of Physics, École Polytechnique Fédérale de Lausanne (EPFL), Lausanne 1015, Switzerland*

(Received 16 November 2023; revised 16 February 2024; accepted 19 March 2024; published 12 April 2024)

We report the experimental observation of large spin-pumping signals in the YIG/Pt system driven by broad-wave-vector spin-wave spin current. 280-nm-wide microwave inductive antennas offer broad-wave-vector excitation, which, in combination with the quasiflatband of YIG, allows a large number of magnons to participate in spin pumping at a given frequency. Through comparison with ferromagnetic resonance spin pumping, we attribute the enhancement of the spin current to the multichromatic magnons. The high efficiency of spin-current generation enables us to uncover nontrivial propagating properties in ultralow power regions. Additionally, our study achieves the spatially separated detection of magnons, allowing the direct extraction of the decay length. The synergistic combination of the capability of broad-wave-vector excitation, enhanced voltage signals, and nonlocal detection provides an alternative avenue for the electrical exploration of spin-wave dynamics.

DOI: 10.1103/PhysRevApplied.21.044024

I. INTRODUCTION

Magnons, the quanta of spin-wave excitations in magnetic materials [1–7], exhibit remarkable characteristics, including the ability to propagate over centimeter distances without experiencing Joule heating dissipation [8–10]. This propagation length significantly surpasses the typical spin-diffusion length by several orders of magnitude [11–13]. The magnon generation, propagation, and detection scheme can play a role in developing efficient magnon spintronic devices, for example, magnon-based logic gates [4,14]. The combination of two physical effects: spin pumping (SP) and the inverse spin Hall effect (ISHE) offers a viable approach. Spin pumping (SP) is the process of generating spin currents $\mathbf{J}_s$ through the excitation of magnons within a ferromagnetic (FM) layer, followed by their injection into an adjacent nonmagnetic (NM) layer [15–17]. Subsequently, the inverse spin Hall effect (ISHE) converts these spin currents into charge currents $\mathbf{J}_c$, more commonly manifesting as voltages [18–20]. Extensive experimental and theoretical efforts have been devoted to understanding the insightful physical mechanisms related to the SP. This includes the investigation of low damping magnetic material systems such as metallic magnets [21–23], organic-based magnets [24], insulating magnets, for example, yttrium iron garnet (YIG) [25], and, more recently, antiferromagnetic hematite [26–28]. Studies have explored the relationship between spin pumping and the thickness of FM and NM materials, as well as the impact of excitation frequency and power [29–31]. Furthermore, there is an emphasis on enhancing interface quality and to further improve the spin-mixing conductance [32–34].

The leading process for SP is the generation of $\mathbf{J}_s$, where the magnitude of $\mathbf{J}_s$ is proportional to the total number of magnons for various wave vectors $\mathbf{J}_s = \hbar \sum_{\mathbf{k}} \mathbf{v}_{\mathbf{k}} n_{\mathbf{k}}$ [25,35,36]. Here, $\mathbf{v}_k = \partial\omega_k/\partial\mathbf{k}$ is the spin-wave group velocity and $n_{\mathbf{k}}$ is the number of magnons. The uniform ferromagnetic resonance (FMR) [32,37–39], standing spin waves [18,40,41], dipolar spin waves [42–46], exchange spin waves excited by an external force [47] and

*Corresponding author: hanchen.wang@mat.ethz.ch
†haiming.yu@buaa.edu.cn
‡These authors contributed equally to this work.

parametrically [48–52] are all employed in the generation of $\mathbf{J}_s$. The majority of previous research has concentrated on the magnons excited with a narrow range of wave vector. This method yields relatively small spin currents $\mathbf{J}_s$, which, when converted to ISHE voltages, are typically in the range of submicrovolts or even less at the power level of several milliwatts. This also limits the efficiency of the detection of spin waves, which has consistently garnered significant attention because of its effective information transfer capabilities [4,53].

In this study, we report a systematic investigation of spin-pumping signals that arise in the YIG/Pt system, in which a nanometer-scale inductive antenna allows the excitation of magnons with a broad range of wave vectors. By varying the angle between the magnetic field and the wave-vector direction, we are able to manipulate the dispersion of the magnons to quasiflatband. The coexistence of these two conditions leads to a large number of magnons participating in the spin-pumping process, resulting in a significant enhancement of ISHE voltages. Furthermore, we find the nearly 100% nonreciprocity of nonlocal ISHE voltage in the configuration close to the case where the angle between the magnetic field and the wave vector is from 60° to 80°. The magnon decay length is experimentally estimated by changing the propagation distances.

II. RESULTS AND DISCUSSION

The sample used in the present study comprises YIG thin films with thickness $t = 80$ nm grown on (111)-oriented gadolinium gallium garnet (GGG) substrates through magnetron sputtering [54]. The postannealing process is performed in an oxygen atmosphere at temperatures ranging from 800 to 900°C. The Gilbert-damping parameter is determined by flipchip ferromagnetic resonance measurements and found to be $\alpha = 5.6 \pm 0.2 \times 10^{-4}$, and the long-range inhomogeneity-caused linewidth is about $\mu_0 \Delta H_0 = 0.42$ mT, as shown in Fig. 5 in Appendix A, consistent with previously reported values [55,56]. The Ti/Au for microwave (MW) antenna is deposited by electron-beam evaporation and heavy metal Pt (7 nm) for detectors is dc-sputter-deposited at room temperature under a working pressure of 2.8 mTorr and a base pressure of 2.0×10^{-7} Torr.

Figure 1(a) depicts the schematic illustration of the conversion mechanism from propagating magnons to charge current. A nanostripline (NSL) antenna is fabricated on the YIG, and the antenna is connected to a vector network analyzer (VNA) via microwave probes. The injected microwave current generates a time-varying oscillating magnetic field ($\mu_0 h_{rf}$) that excites magnons and then propagates $s = 2$ μm to the Pt detector. Subsequently, spin-wave spin current is converted into a charge current locally at the detection part. The Pt bar is connected to a

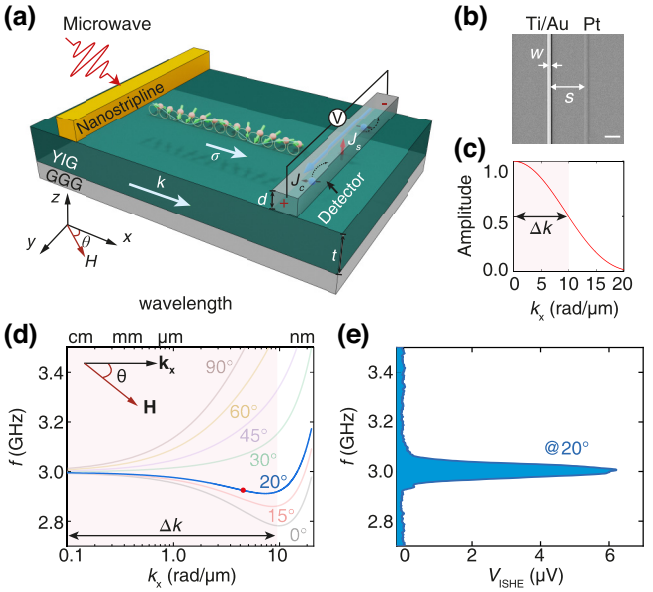

FIG. 1. (a) Schematic illustration of the broad-wave-vector SP setup. Magnons in the YIG layer are excited using a microwave flowing in a nanostripline antenna. A nanovoltmeter is connected to the Pt bar to detect voltage induced by the charge currents $\mathbf{J}_c$. θ denotes the in-plane angle between the wave vector k and the applied external field $\mathbf{H}$. (b) The SEM image of the antennas, where the scale bar is 1 μm. (c) Broad-wave-vector distribution calculated by the width of NSL using FFT. The half value of the maximum wave-vector excitation, represented by Δk, is chosen to an effective range of the wave vector. (d) The magnon dispersion and the mechanism of the broad-wave-vector spin-pumping process at flatband scenario (20°) and other angles. The pink shadow is the effective range of broad-wave-vector excitation. (e) The propagating magnons detected by ISHE at the power of $P_{MW} = 63$ μW (−12 dBm) and $\theta = 20°$ with $\mu_0 H = 51$ mT.

nanovoltmeter to detect ISHE voltage (V_{ISHE}). The magnon dispersion of an 80-nm-thick YIG film at different angles, calculated by the dipolar-exchange spin-wave theory [57], is presented in Fig. 1(d). We find that when a magnetic field $\mu_0 H$ is applied at a 20° angle with respect to wave vector, a near quasiflatband of magnons [58–61] appears within the wave-vector range from 0 to 10 rad/μm. The 280-nm-wide NSL [Fig. 1(b)] offers the ability of the broad range of wave-vector excitation. Broad-wave-vector distribution calculated by the width of NSL using fast Fourier transform (FFT) is shown in Fig. 1(c). The half-value of the maximum wave-vector excitation is chosen to be an effective width of wave vector, represented by $\Delta k = 10$ rad/μm, which is enough to cover the wave vector associated with the flat-band magnons. As the excitation frequency approaches a specific value close to the flat-band frequency, a significant population of magnons with various wave vectors get excited and participate in the process of generating spin current after propagating to the detection part. The dc component of the

spin current for each wave vector at the interface can be described as [19,62,63]

$$\mathbf{J}_s^k = \frac{\hbar f}{2} \mathrm{Re}\left(g_{\uparrow\downarrow}\right) P \sin^2 \phi_k, \tag{1}$$

where f is the excitation frequency, $\mathrm{Re}\left(g_{\uparrow\downarrow}\right)$ is the real part of the interfacial spin-mixing conductance $g_{\uparrow\downarrow}$, ϕ_k is the precession cone angle of spin waves with wave vector k, and P is a factor arising from the ellipticity of the magnetization precession. Considering the number of magnons $n_k \propto \phi_k^2 \propto \mathbf{J}_s^k$ [64], the total spin current generated by magnons with different wave vectors k can be represented as $\mathbf{J}_s^{\mathrm{tot}} = \sum_{k_i} \mathbf{J}_s^{k_i}$, where k_i is sweeping from 0 to Δk. Because of ISHE, the spin current can be converted into charge current $\mathbf{J}_c = (2e/\hbar)\Theta_{\mathrm{SH}}[\mathbf{J}_s^{\mathrm{tot}} \times \sigma]$, and is detected as a voltage via Pt bar. Here, Θ_{SH} represents the spin Hall angle, and σ is the spin-polarization direction aligned with the magnetization $\mathbf{M}$. Finally, the ISHE-induced charge current results in charge accumulation at the two ends of the detector, which can be detected by a nanovoltmeter as the ISHE voltage [19,65–67]:

$$V_{\mathrm{ISHE}} = \frac{2e\Theta_{\mathrm{SH}}}{\hbar} \frac{1}{\sigma_N d_N} \lambda_{\mathrm{SD}} \tanh\left(\frac{d_N}{2\lambda_{\mathrm{SD}}}\right) L \mathbf{J}_s^{\mathrm{tot}}, \tag{2}$$

where the electron charge e, charge conductivities and the thickness of the normal metal layer σ_N and d_N, the spin-diffusion length λ_{SD}, and the effective length L of spin pumping. Figure 1(e) shows the V_{ISHE} spectrum of propagating magnons recorded at a distance $s = 2$ μm, $\mu_0 H = 51$ mT with microwave power $P_{\mathrm{MW}} = 63$ μW. We rule out the possibility of the voltage signal contribution from the spin rectification effect imposed by spin Hall magnetoresistance [68,69] or spin Seebeck effect [70] (see Fig. 6 in Appendix B). Nevertheless, it is essential to highlight that the excitation of spin waves by the platinum strip may occur due to the electromagnetic coupling between these two parallel conductors within the system, of which the strength diminishes significantly with larger separations between the antenna and detector. Further distance-dependent measurement (Fig. 4) and nonreciprocal feature (Fig. 3) reveal that this additional effect does not substantially alter the key observations presented in this work. Under the simultaneous fulfilment of a broad-wave-vector excitation and flatband magnon dispersion, the increased population of magnons leads to the large V_{ISHE}.

To attribute the multichromatic magnons to the enhancement of the spin current, we conduct V_{ISHE} measurements using uniform spin pumping ($V_{\Delta k=0}$) (see setup information in Fig. 7 in Appendix C) for comparison with broad-wave-vector spin pumping ($V_{\Delta k\neq 0}$). The excitation power is 10 mW for $\Delta k = 0$ measurements and 63 μW for $\Delta k \neq 0$ measurements, respectively, maintaining a linear precession region [see Figs. 2(b) and 2(c)]. We fix the

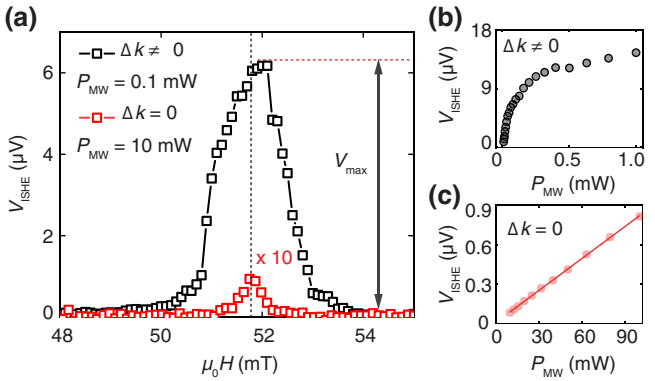

FIG. 2. (a) V_{ISHE} as a function of the field at $f = 3$ GHz for broad-wave-vector spin pumping ($\Delta k \neq 0$ rad/μm) and uniform spin pumping ($\Delta k = 0$ rad/μm) with excitation powers of 63 μW and 10 mW, respectively. V_{max} denotes the maximum voltage. (b) Excitation power dependence of maximum value in voltage spectra for $\Delta k \neq 0$ rad/μm and (c) for $\Delta k = 0$ rad/μm, respectively. The red solid line is the linear fitting result.

excitation frequency at 3 GHz and sweep the magnetic field to observe the resonance peaks. The V_{ISHE} curves are depicted in Fig. 2(a), where the maximum voltage V_{max} for $V_{\Delta k\neq 0}$ is 6.2 μV and the black dot line denotes the ferromagnetic resonance field $\mu_0 H_{\mathrm{FMR}}$. The maximum value for $V_{\Delta k=0}$ at $\mu_0 H_{\mathrm{FMR}}$ is 0.09 μV. Compared to the measurements with $\Delta k = 0$, the voltage observed in the $\Delta k \neq 0$ measurements shows a significant enhancement. In Eq. (2), one can find that there are many parameters related to the V_{ISHE}. The $\lambda_{\mathrm{SD}} \approx 8$ nm for Pt, surpasses d_N, where d_N is 5 nm for $\Delta k = 0$ and 7 nm for $\Delta k \neq 0$ measurements. Considering that the term $\lambda_{\mathrm{SD}}/d_N \tanh(d_N/2\lambda_{\mathrm{SD}})$ is essentially constant for $\lambda_{\mathrm{SD}} > d_N$ due to the limitation of film thickness [65], it has a feeble effect on the measured voltage. Consequently, we have

$$\frac{V_{\Delta k\neq 0}}{V_{\Delta k=0}} = \frac{L_{\Delta k\neq 0}}{L_{\Delta k=0}} \frac{\sum_{k_i} \mathbf{J}_s^{k_i}}{\mathbf{J}_s^0},$$

where $\mathbf{J}_s^0$ is the spin current generated by uniform spin pumping. One needs a factor δ to meet $\sum_{k_i} \mathbf{J}_s^{k_i} = \delta \mathbf{J}_s^k$, by which the whole contribution of the broad-wave-vector magnons may be qualitatively extracted from the measured value of the spin-pumping voltage. According to Eq. (1), $\mathbf{J}_s$ is the function of the cone angle ϕ. ϕ is generally small (1° or less) and can be expressed as $\sin\phi_k \approx \phi_k = \gamma \mu_0 h_{\mathrm{rf}}/4\pi\alpha_{\mathrm{eff}}^k f$, where α_{eff}^k is the wave-vector-dependent effective Gilbert damping. Combining it with δ, we have

$$\delta = \frac{V_{\Delta k\neq 0}}{V_{\Delta k=0}} \frac{L_{\Delta k=0}}{L_{\Delta k\neq 0}} \left(\frac{\mu_0 h_{\mathrm{rf}}^{\Delta k=0}}{\mu_0 h_{\mathrm{rf}}^{\Delta k\neq 0}}\right)^2 \left(\frac{\alpha_{\mathrm{eff}}^k}{\alpha_{\mathrm{YIG/Pt}}}\right)^2. \tag{3}$$

We normalize the parameters' spin-pumping effective length L, $\mu_0 h_{\mathrm{rf}}$, and effective damping α for $\Delta k \neq 0$ and

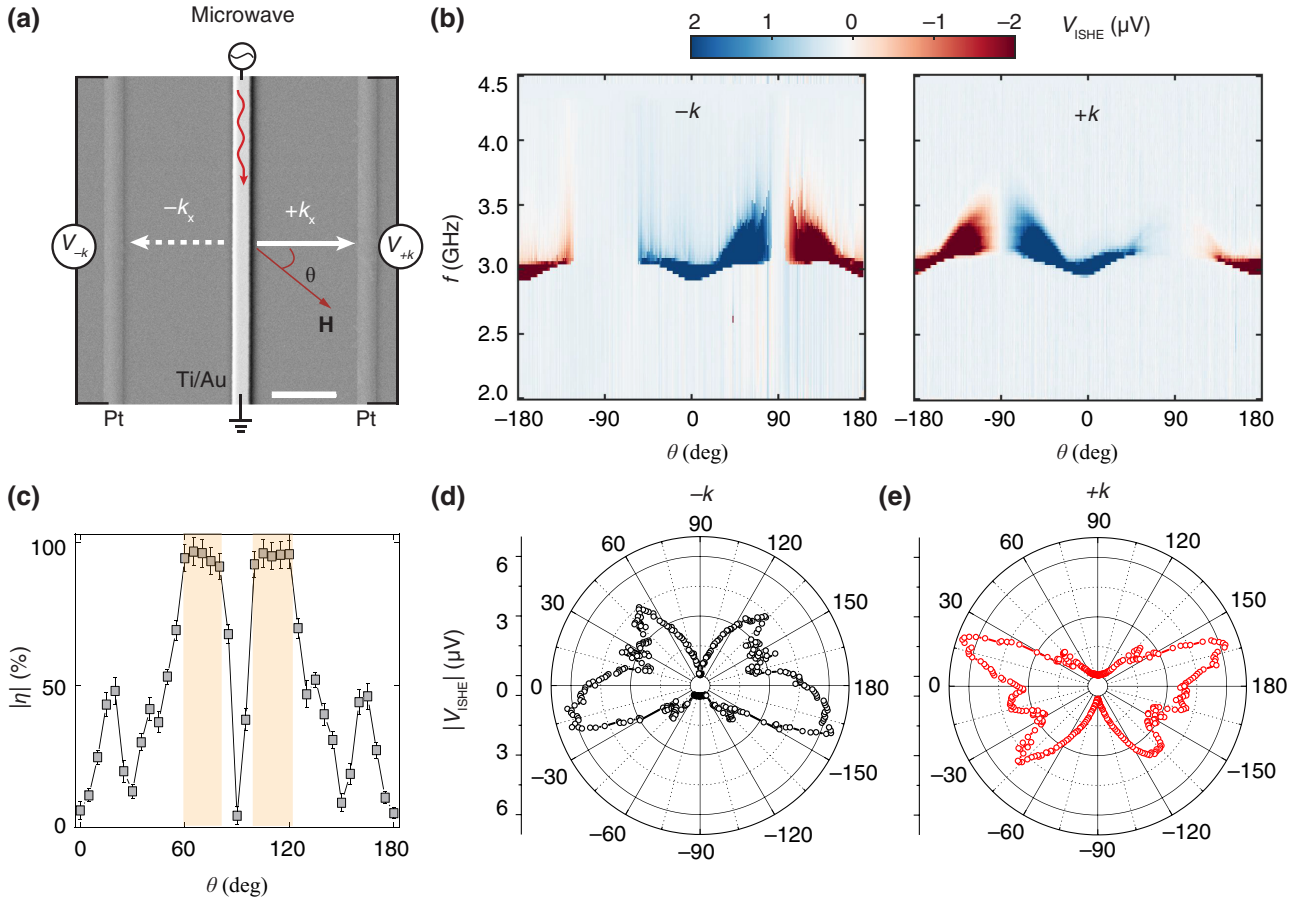

FIG. 3. (a) The device wherein two identical Pt strips are placed symmetrically in the left (V_{-k}) and right (V_{+k}) sides of NSL with same propagation distance 2 μm, where scale bar is 1 μm. (b) Angle-dependent spectra of V_{ISHE} for magnons with opposite propagating directions at $\mu_0 H = 52$ mT and $P_{MW} = 63$ μW. (c) θ dependence of V_{ISHE} nonreciprocity η. (d) Angular dependence of the absolute voltage with the extraction of maximum V_{ISHE} values at each angle from -k spectrum and (e) from +k spectrum.

$\Delta k = 0$ measurements. Assuming that the broad-wave-vector magnons are uniformly excited along the length of the NSL, we can approximate the length of the Pt detector as $L_{\Delta k \neq 0}$, which is approximately 100 μm. Considering a 120-nm-thin NSL of width ω with its center at $x = z = 0$,

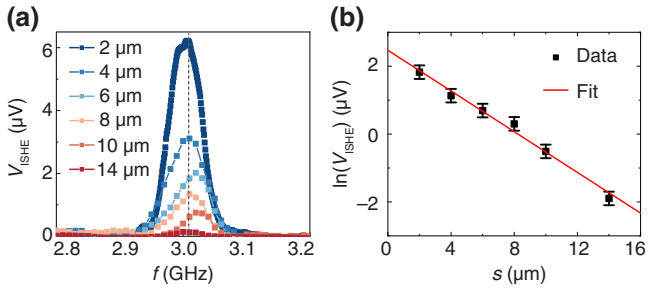

FIG. 4. (a) Frequency-dependent V_{ISHE} lineplots measured in devices with different propagation distances at $\mu_0 H = 52.2$ mT, $\theta = 20^\circ$, and $P_{MW} = 63$ μW. The gray dash line corresponds to frequency $f = 3$ GHz. (b) The dependence of the logarithm of ln(V_{ISHE}) as a function of propagation distance at 3 GHz. The red line is the linear fitting using Eq. (7).

the electromagnetic field distribution is calculated, and it reveals the maximum $\mu_0 h_{rf}$ value of 0.93 mT at the central position with input $P_{MW} = 63$ μW [see Fig. 8(a) in Appendix D]. The $L(\mu_0 h_{rf})^2$ for $\Delta k \neq 0$ is estimated to 0.09 mT^2 mm. The value $L(\mu_0 h_{rf})^2 = 0.13$ mT^2 mm is calculated for $\Delta k = 0$ by integrating over the effective region influenced by the antenna's field when $P_{MW} = 10$ mW [see Fig. 8(b) in Appendix D]. From Fig. 2(a), for $V_{\Delta k \neq 0}$, the magnetic field $\mu_0 H$ corresponding to the V_{max} is 52.2 mT. The frequency f of spin wave with wave vector k [57,71–73]:

$$f = \frac{|\gamma|\mu_0}{2\pi}\left[\left(H + \frac{2A}{\mu_0 M_s}k^2\right) \times \left(H + \frac{2A}{\mu_0 M_s}k^2 + FM_s\right)\right]^{\frac{1}{2}}, \tag{4}$$

$$F = 1 - \left(1 - \frac{1 - e^{-kt}}{kt}\right)\cos^2\theta + \left(\frac{M_s}{H + \frac{2A}{\mu_0 M_s}k^2}\right) \times \left(\frac{1 - e^{-2kt}}{4}\right)\sin^2\theta, \tag{5}$$

where $|\gamma| = 2\pi \times 28$ GHz/T is the gyromagnetic ratio, $A = 3$ pJ/m is the exchange stiffness constant [73], t is the thickness of the YIG layer, $\mu_0 M_s$ about 0.17 T is the saturation magnetization of YIG, and F is the dipolar array factor. When excitation frequency $f = 3$ GHz, the maximum k corresponding to 52.2 mT is 2.5 rad/μm (see Fig. 9 in Appendix E). Given the varying damping between high-k magnons and $k = 0$ magnons, which tends to increase with increasing the wave vector, we derived the effective damping α_{eff} from the wave-vector-dependent relaxation time $\tau(k) = [2\pi\alpha_{\text{eff}} f(k)]^{-1}$ [72,74]. The effective damping α_{eff}^{k} is approximately 6.5 × 10-4 when k is 2.5 rad/μm. The damping of YIG/Pt bilayer $\alpha_{\text{YIG/Pt}}$ for $\Delta k = 0$ measurements is 7.8×10^{-4} (see Fig. 10 in Appendix F). Taking into account the combined influence of

$$\frac{L_{\Delta k\neq 0}}{L_{\Delta k=0}}\left(\frac{h_{\text{rf}}^{\Delta k\neq 0}}{h_{\text{rf}}^{\Delta k=0}}\right)^2\left(\frac{\alpha_{\text{YIG/Pt}}}{\alpha_{\text{eff}}^{k}}\right)^2,$$

it gives a ratio of nearly 1, compared with the ratio of the maximum voltage observed in the experiment $(V_{\Delta k\neq 0})/(V_{\Delta k=0}) = 68.9$, there should have a factor of 69.0 from δ. However, it is worth noting that, in some cases, it is also known that the attenuation of homogeneous precession in YIG films can exceed the attenuation of short-wavelength magnons, which is explained by both the better coupling of such precession with electromagnetic waves in the environment and the stronger contribution of two-magnon scattering [75]. For example, Ref. [75] claims the lowest damping of spin waves is found at the wave vector of about 10 rad/μm, indicating that the ratio δ can be even larger than 69.0 if the effective damping at high k is overestimated. The evolution of the V_{ISHE} signals as a function of wave vector for excitations also demonstrates the effectiveness of broad-wave-vector spin pumping (see Fig. 11 in Appendix G). Figures 2(b) and 2(c) summarize the maximum value in a voltage spectrum under different excitation powers for $\Delta k \neq 0$ and $\Delta k = 0$, respectively. The spin pumping with $\Delta k = 0$ exhibits a linear relationship with P_{MW} up to the maximum microwave power of 100 mW [Fig. 2(c)]. In comparison, the signal of spin pumping with $\Delta k \neq 0$ maintains in the linear region only up to 0.1 mW. This demonstrates that the spin pumping with $\Delta k \neq 0$ requires much lower microwave power than the $\Delta k = 0$ to achieve the same spin current, and also a much easier step into the nonlinear regime [76]. To gain a comprehensive understanding of the voltage saturation feature observed in the nonlinear regime in Fig. 2(b), we conduct an additional power-dependent measurement with sweeping the external magnetic field from −100 to 100 mT, keeping the frequency fixed at 3 GHz. The measurement results reveal that as the power exceeds 0.1 mW and the main mode enters the nonlinear regime, the parametric mode becomes more pronounced. Based on this power-dependent analysis, we posit that the voltage saturation of the main mode primarily stems from magnon-photon and magnon-magnon interactions, particularly in nonlinear processes like parametric pumping. To further optimize spin-current generation efficiency, future experimental endeavors could explore methods to mitigate nonlinear effects in the system. This avenue not only promises enhanced spin-current generation under high-power excitation but also serves as a valuable platform for delving into open questions surrounding the nonlinear saturation of spin pumping and inverse spin Hall effect processes. More information can be found in Fig. 12 in Appendix H.

In order to gain more insight into the magnon-driven ISHE, we study its angular dependence (Fig. 3) with a MW power of 63 μW. First, two identical Pt detectors are positioned on the two opposite sides of the NSL with a separated distance of 2 μm. At 52 mT, we record the angle-dependent spectra V_{ISHE} for both $-k$ and $+k$ magnons [Fig. 3(b)] by rotating the in-plane magnetic field. We extract the V_{max} at each angle [Figs. 3(d) and 3(e)]. The output voltage exhibits an asymmetric dependency resembling a butterfly pattern. At the excitation part, the varying microwave absorption capability of the magnetic material under different θ leads to an angular dependency in the NSL's excitation efficiency, described using $A\sin^2\theta + B$ [28]. At the detection part, the ISHE follows a $\cos\theta$ law [77]. Merely considering the angular dependencies of excitation and detection does not align with the experimental outcomes (see Fig. 13 in Appendix I). Therefore, we consider that the propagation of magnons contributes to additional asymmetry. As θ gradually rotates from 0° towards 90°, the spin-wave mode transitions from a volume mode to a surface mode, exhibiting noticeable nonreciprocal propagating (see Fig. 14 in Appendix J). We quantify the V_{ISHE} nonreciprocity in terms of the ratio,

$$\eta = \frac{V_{-k} - V_{+k}}{V_{-k} + V_{+k}}, \tag{6}$$

where $|\eta| = 100\%$ indicates perfect unidirectional V_{ISHE} detection. We show the $|\eta|$ extracted from the experiments as a function of θ in Fig. 3(c), which exhibits nearly 100% when θ is rotated between 60° and 80°. Due to the finite thickness of YIG, the amplitude distribution of precession profile along the thickness direction is nonuniform, particularly in the context of dipolar-exchange spin waves. Consequently, the Damon-Eshbach (DE) mode has the capability to induce a spin-wave spin current at the top or bottom surfaces of the material. As an illustrative example, when considering the case of $+k$ magnons, apart from the detection restrictions causing V_{ISHE} signal of zero within the DE mode, in the vicinity of the DE mode at angles θ, roughly between 60° and 80°, a close-to-zero V_{ISHE} can also be observed. This phenomenon underscores

the interfacial nature of the spin-pumping process, implying that the majority of magnons likely propagate along the bottom surface. This, in turn, suggests that the primary source of the spin current is surface-bound magnons, as opposed to magnons traversing the entire thickness of the material. The angle-dependent measurement results in nonlinear regime (1.0 mW) can be found in Fig. 15 in Appendix K.

The spatially separated detection enables us to measure the decay length of magnons. Consequently, keeping the excitation NSL unchanged, we conduct measurements to explore the V_{ISHE} dependence on distance. Figure 4(a) shows the V_{ISHE} recorded at $\mu_0 H = 52.2$ mT with propagation distances $s = 2, 4, 6, 8, 10$, and 14 μm. The longer the propagation distance is, the less magnons can then be detected, and therefore the weaker ISHE signal. With a fixed frequency at 3 GHz, the maximum values of V_{ISHE} at different propagation distances are extracted. The dependence of the logarithm of $\ln(V_{\mathrm{ISHE}})$ as a function of s is shown in Fig. 4(b) and fitted them by,

$$\ln\left(\frac{V_{\mathrm{ISHE}}}{C_{\mathrm{m}}}\right) = -\frac{s}{\lambda_{\mathrm{m}}}, \tag{7}$$

where C_{m} and λ_{m} are distance-independent prefactor and magnon decay length, respectively. By fitting the results of the experiment, the decay length λ_{m} is extracted about 3.3 ± 0.3 μm, which compares well to previous experimental results [78,79]. Combining the estimated decay length with the effective Gilbert damping, we can roughly estimate the corresponding spin-wave group velocity by using $|v_{\mathrm{g}}| = 2\pi\alpha_{\mathrm{eff}} f\, \lambda_{\mathrm{m}}$, which is about 0.037–0.044 km/s. This estimated spin-wave group-velocity value range corresponds to a wave-vector range from 5.22 to 5.56 rad/μm at 20° [center of the broad range of wave vector provided by the antenna as shown by the red point in Fig. 1(d)], which is calculated by Eqs. (4) and (5) and $v_{\mathrm{g}} = 2\pi\, \partial f\, /\partial k$. The spin-wave group velocity as a function of wave vector at 20° can be found in Fig. 16 in Appendix L. Decay length $\lambda_{\mathrm{m}} = v_{\mathrm{g}}/2\pi\alpha f$, is largest for magnons with high group velocity or small damping. Unlike the conventional uniform excitation SP, which necessitates the deposition of Pt on the entire surface of the YIG, creating a YIG/Pt heterostructure, our approach obviates this requirement, thus mitigating the increase in YIG's damping coefficient. This approach allows us to preserve a relatively large decay length.

In this study, a thick YIG (80 nm) thin film is employed to showcase the technique for electrically detecting magnon dynamics. Further experimental exploration using thinner samples would be both promising and intriguing. As the YIG thickness decreases, the dipolar interaction is suppressed, providing a relatively broader angle range to support the quasi-flat-band scenario. Furthermore, the reduction in thickness leads to higher frequencies for the high-order magnon bands, effectively suppressing magnon-magnon and magnon-photon interactions, particularly in the nonlinear regime. Except for the backward volume mode, spin waves propagating at other angles exhibit surface-mode profiles along the thickness direction due to dipolar interaction. This indicates that magnon spin currents, further pumped into the detector, decay from the surfaces. Decreasing the YIG thickness results in a more homogeneous profile, suggesting that magnon spin currents at different positions along the thickness experience less dissipation towards the top surface. Consequently, they are more efficiently converted into charge current in the detector through the inverse spin Hall effect. In other words, the spin-pumping efficiency, especially for magnon spin currents with surface features, is enhanced in thinner samples [80]. In addition, it is worthwhile to discuss the significance of material selection (conductive and insulating) on measured results and the potential for device miniaturization. In the case of insulating materials, such as garnets, the outcomes are primarily shaped by the diverse intrinsic magnon dispersions arising from distinct magnetic parameters, including magnetic anisotropy, Dzyaloshinskii-Moriya interaction, saturation magnetization, and exchange stiffness. In conducting materials, additional factors may impact detected results, including issues like short circuits between the spin-wave waveguide and detector, spin rectification, significant crosstalk, and self-pumping induced by self-torque. Despite these supplementary effects, the results are still predominantly determined by intrinsic magnon dispersions. Regarding the potential for device miniaturization, we posit that common challenges across all materials include on-chip Joule heating induced by the antenna and variations in interfacial spin-mixing conductance between materials and the detector. To downscale device size effectively, optimizing the excitation efficiency of short-wavelength spin waves becomes crucial, particularly for materials with higher magnon gaps and saturation magnetization, which require higher frequencies. Moreover, spatially separated detection offers distinct advantages in terms of facilitating gating and manipulating spin waves. When combined with the efficient excitation of magnons, it paves the way for another route in the generation, propagation, and detection of spin currents, which is essential for the development of magnon-based logic devices.

III. CONCLUSION

In conclusion, we experimentally observe significant voltage signals from broad-wave-vector excitation flatband magnons spin pumping in thin YIG films. The utilization of nanoscale stripline enables efficient angular momentum transfer of flatband magnons across a broad range of wave vectors into the spin current. The generation of

spin-wave spin current with a broad range of wave vectors is observed to be over 69.0 times greater than that associated with a single wave vector. We also clarify that spin pumping primarily originates from magnons at the surface rather than spanning the full thickness, supported by the nonreciprocal propagation of magnetostatic surface spin waves. The ability of unidirectional detection of V_{ISHE} in combination with long-distance propagating magnons can become a key functionality in reconfigurable nanomagnonic logic and computing devices. Our finding allows for the downsizing of input microwave power and spin-pumping structures, all while preserving adequately robust signals and the dynamic properties of spin waves. The periodic Dzyaloshinskii-Moriya coupling or moiré pattern also induced flatband [58–61]. In the future, combining this with broad-wave-vector spin pumping could offer insights into the spin-wave dynamics regime.

ACKNOWLEDGMENTS

We thank G.E.W. Bauer, P. Gambardella, K. Yamamoto, and S. Maekawa for their helpful discussions. We wish to acknowledge the support by the National Key Research and Development Program of China Grant No. 2022YFA1402801, by NSF China under Grants No. 12074026, No. 52225106, and No. U1801661, and by Shenzhen Institute for Quantum Science and Engineering, Southern University of Science and Technology (Grant No. SIQSE202007). H.W. acknowledge support by China Scholarship Council (CSC) under Grant No. 202206020091 and W.L. acknowledge support by an ETH Zurich Postdoctoral Fellowship (21-1 FEL-48).

APPENDIX A: FIELD-DEPENDENT FLIPCHIP FMR SPECTRA AND DAMPING ESTIMATION

In the flipchip measurement, the submillimeter size coplanar waveguide (CPW) antenna is used to excite and detect the resonance of the whole chip, to characterize the FMR feature of the YIG sample. The in-plane external magnetic field is applied perpendicular to the wave-vector direction, a field-dependent spectra is obtained as presented in Fig. 5(a). Based on the FMR spectra, the linewidths δf at different excitation frequencies are extracted by fitting with a Lorentz function [Fig. 5(b)]. The damping parameter $\alpha = 5.6 \pm 0.2 \times 10^{-4}$ of the film is given by the linear fitting using the following Eq. (A1) [81]:

$$\delta f = \frac{|\gamma|}{2\pi}\mu_0 \Delta H_0 + \frac{2}{\sqrt{3}}\alpha f\,, \tag{A1}$$

where $|\gamma| = 2\pi \times 28$ GHz/T is the gyromagnetic ratio, $\mu_0 \Delta H_0 = 0.42$ mT is the film inhomogeneity linewidth. Then we performed the superconducting quantum interference device (SQUID) measurement to obtain the hysteresis loop with applying in-plane external magnetic field. The sample size is 3 mm × 4 mm × 80 nm corresponding to 9.6 cm^3 volume. After dividing the total magnetization by the volume of the sample, the saturation magnetization $\mu_0 M_s$ of this chip is herein estimated at about 170 mT.

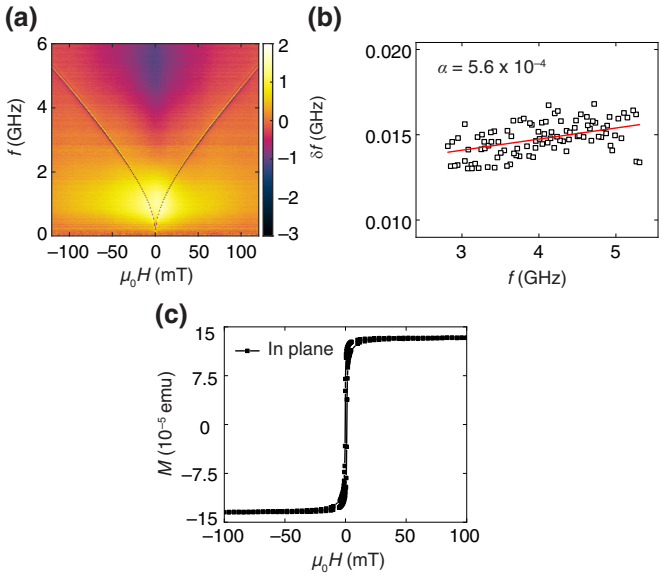

FIG. 5. (a) The FMR reflection spectra measured by flipchip technique with in-plane magnetic field. (b) The extracted FMR linewidths δf as a function of the different excitation frequencies. The red solid line is the damping fitting based on Eq. (A1). (c) The magnetic hysteresis loop measured with applying in-plane magnetic field.

APPENDIX B: MAGNON PROPAGATION SPECTRA DETECTED BY ISHE

Maintaining propagation distance $s = 2$ μm, fixed power $P_{\mathrm{MW}} = 63$ μW, sweeping in-plane magnetic field at different frequencies, we get a field-dependent mode as shown in Fig. 6(a). Reversing the measured signal's polarity with changing magnetic field direction and no steplike line shape at zero field eliminates possible thermoelectric effects [Fig. 6(b)]. To exclude the contribution from the spin rectification effect imposed by spin Hall magnetoresistance (V_{SMR}), in the following, we also replace the Pt detection antenna with W, as shown in Fig. 6(c). Since V_{SMR} is proportional to the square of the spin Hall angle ($V_{\mathrm{SMR}} \propto \Theta_{\mathrm{SH}}^2$) [82], a dominant V_{SMR} contribution would result in positive voltage signals for both YIG | Pt and YIG | W, despite the opposite spin Hall angles of Pt and W. The striking feature observed here is the opposite signs, proving that the signal mainly originates from V_{ISHE} ($V_{\mathrm{ISHE}} \propto \Theta_{\mathrm{SH}}$).

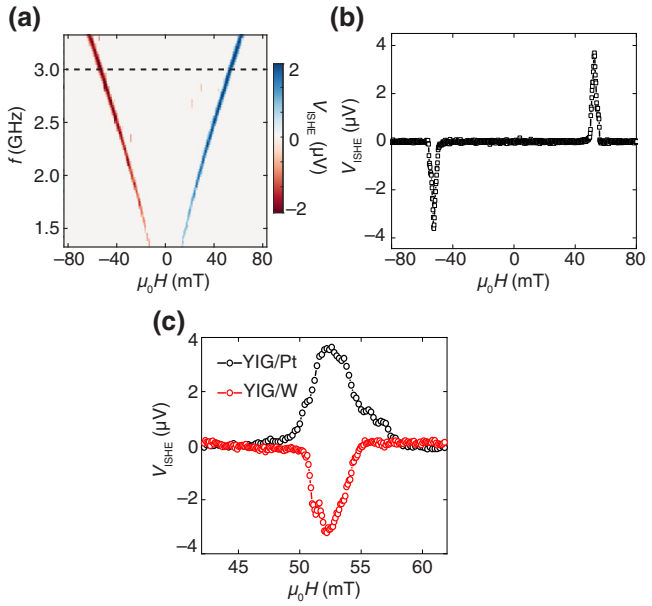

FIG. 6. (a) The propagating magnon spectrum detected by ISHE at power $P_{mW} = 63\ \mu W$ and $\theta = 0^\circ$ with field sweep from negative to positive. (b) Single line cuts extracted from (a) at frequency $f = 3$ GHz. (c) Comparison of spin-pumping voltage measured for YIG | Pt and YIG | W.

APPENDIX C: SCHEMATIC LAYOUT OF THE UNIFORM SPIN-PUMPING EXPERIMENTAL SETUP

We conduct V_{ISHE} measurements using the FMR ($\Delta k = 0$) technique for comparison with broad-wave-vector magnon spin pumping ($\Delta k \neq 0$). Our $\Delta k = 0$ measurements are performed on a YIG (80)/Pt (5) bilayer sample approximately 5×5 mm^2. The signal line width is 75 μm with a 140-μm gap between the signal and ground lines for coplanar waveguide (CPW). The sample was positioned above the CPW with an external magnetic field applied on the y axis, while the ISHE voltage was measured across the whole chip at two sides in x-axis direction, as illustrated in Fig. 7.

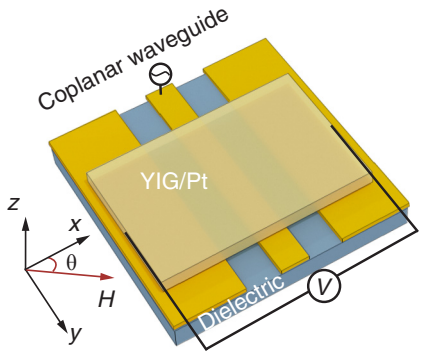

FIG. 7. Schematic layout of the uniform spin-pumping experimental setup. The microwave flowing in the coplanar waveguide excites uniform precession of YIG/Pt bilayer and then generates spin current. Electrodes attached to the Pt layer are used to detect the voltage resulting from the charge current.

APPENDIX D: SPATIAL DISTRIBUTION OF THE $\mu_0 h_{rf}$ COMPONENTS FOR NSL AND CPW

For comparison of the ISHE voltage contribution from the microwave field, we have calculated the $\mu_0 h_{rf}$ components of the NSL and CPW when input power equals 63 μW and 10 mW, respectively. Considering a nanostripline with a thickness of $d = 120$ nm and width of $w = 280$ nm along the y axis, whose center is at $x = y = 0$. The $\mu_0 h_{rf}$ field at point A(x_0, z_0) is given by Eqs. (D1) and D2 [83]:

$$\mu_0 h_x(x_0, z_0) = \eta \int_0^d \left[\int_0^{w/2+x_0} \frac{z_0 + z}{p^2 + (z_0 + z)^2} dp - \int_0^{x_0 - w/2} \frac{z_0 + z}{p^2 + (z_0 + z)^2} dp \right] dz, \quad \text{(D1)}$$

$$\mu_0 h_z(x_0, z_0) = \eta \int_0^d \left[\int_0^{w/2+x_0} \frac{-p}{p^2 + (z_0 + z)^2} dp - + \int_0^{x_0 - w/2} \frac{p}{p^2 + (z_0 + z)^2} dp \right] dz, \quad \text{(D2)}$$

where η is $2\pi j / \mu_0$, j is current density and μ_0 is vacuum permeability. With the impedance Z_0 equal to 107 Ω for NSL, we calculated the $\mu_0 h_x$ and $\mu_0 h_z$ components of the magnetic fields induced by the microwave current at the half thickness position of the film as shown in Fig. 8(a), which give a $\mu_0 h_x$ field of 0.93 mT at the center and inhomogeneous amplitudes of excitation in the z direction. Considering the effective detecting length of Pt $L_{\Delta k \neq 0} = 100$ μm, the $L_{\Delta k \neq 0} (\mu_0 h_{rf}^{\Delta k \neq 0})^2$ is 0.09 mT^{2}mm. For the $\mu_0 h_{rf}$ component of CPW, electromagnetic simulations were performed using HFSS 2022 with the following parameters. We used the same CPW dimension with the experiment: $S = 75$ μm, $G = 200$ μm, and spaced 140 μm, apart with an Au thickness of 120 nm. The thickness of the YIG film was taken as 80 nm with relative dielectric constant $\epsilon_r = 15$, and for the GGG substrate, we used a thickness of 500 μm with $\epsilon_r = 12$. We performed the simulation at a frequency of 10 GHz. Figure 8(b) shows the $\mu_0 h_x$ component in the (x, y) plane on top of the YIG surface ($z = 10$ μm). The use of an input power of 10 mW with Z_0 of 50 Ω, would give a maximum field $\mu_0 h_x$ about 0.7 mT. Therefore, for the CPW antenna, the $L_{\Delta k=0} \times (\mu_0 h_{rf}^{\Delta k=0})^2$ is 0.13 mT^2 μm.

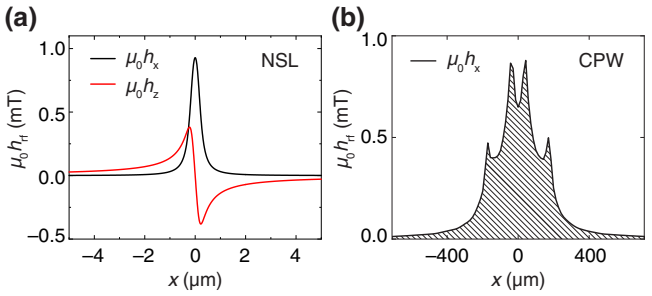

FIG. 8. (a) Spatial distribution of the $\mu_0 h_x$ and $\mu_0 h_z$ components of the magnetic fields induced by the microwave current flowing through a 280-nm-wide NSL antenna with $P_{MW} = 63$ μW. (b) Spatial distribution of the $\mu_0 h_x$ component of the magnetic fields induced by the microwave current flowing through a 75-μm-wide CPW antenna with $P_{MW} = 10$ mW.

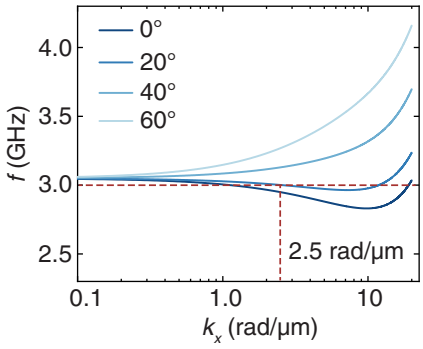

FIG. 9. Theoretically calculated dispersions of 80-nm-thick YIG film at different angle θ. The red vertical dashed line implies the crossing wave vector when excitation frequency is at 3 GHz.

APPENDIX E: DISPERSION FOR 80-NM-THICK YIG FILM AT $\mu_0 H = 52.2$ mT

Figure 9 presents the dispersion calculated by Eq. (5) in the main text with in-plane magnetic field $\mu_0 H = 52.2$ mT. From dispersion, we find that keeping the excitation frequency at 3 GHz, the maximum wave vector is 2.5 rad/μm when $\theta = 20°$.

APPENDIX F: THE DAMPING FITTING OF YIG/PT HETROSTRUCTURE

Figure 10 presents FMR data of the YIG/Pt bilayer. The linear fitting yields damping $\alpha = 7.8 \times 10^{-4}$. Compared with bare YIG, damping is enhanced.

APPENDIX G: WAVE-VECTOR-DEPENDENT INVERSE SPIN HALL VOLTAGE

The evolution of the V_{ISHE} signals as a function of wave vectors has been studied. As an example, keeping propagation distance $s = 2$ μm, the V_{ISHE} recorded for a series of NSL with different widths ω are shown in Fig. 11(a). Δk for 2, 2, and 100 μm NSL antenna is 1.5, 0.15, and 0.03 rad/μm, respectively [Fig. 11(b)]. With increasing ω, the range of excitation wave vector Δk decreases, as does the maximum value of the V_{ISHE}. When we change the excitation antenna from an NSL excitation antenna to a coplanar waveguide (CPW) configuration, maintaining the same signal line width (0.28 μm as in the NSL configuration described in the main text), the resulting V_{ISHE} signal decreases by nearly half. A comparison with the wave-vector distribution of NSL in Fig. 1(c) of the main text reveals that the wave vector for CPW exhibits finite values [Fig. 11(d)]. However, for NSL, the wave vectors are excited more broadly. With the same excitation power at a fixed frequency, for CPW, the number of magnons participating in generating spin current decreases, and consequently, so does V_{ISHE}.

APPENDIX H: POWER-DEPENDENT PUMPING VOLTAGE RESULTS AT 3.0 GHZ

To gain a comprehensive understanding of the voltage saturation feature observed in the nonlinear regime in Fig. 2(b) in the main text, we conduct an additional power-dependent measurement with sweeping the external magnetic field from −100 to 100 mT, keeping the frequency fixed at 3 GHz. The voltage spectra [Fig. 12(a)] reveal that as the power exceeds 0.1 mW (−10 dBm) and the main mode enters the nonlinear regime, the parametric mode becomes more pronounced. In addition, we extract the voltage strengths of each mode as a function of power, illustrated in Fig. 12(b). It is observed that as the power increases (beyond 0.1 mW), the main mode (f mode) experiences a slight saturation, while the strengths of the nonlinear mode ($2f$ mode) exhibit a sudden increase. Based on this power-dependent analysis, we posit that the voltage saturation of the main mode primarily stems from magnon-photon and magnon-magnon interactions, particularly in nonlinear processes like parametric pumping.

APPENDIX I: ANGLE DEPENDENCE OF ISHE MULTIPLIED BY THE ANGLE DEPENDENCE OF POWER ABSORPTION

To comprehend the anisotropy of voltage values at different angles, we computed the antenna excitation efficiency and the ISHE detection efficiency's impact on the ISHE voltage. Taking into account that for a magnetic field applied at an angle θ from the wave vector, the absorbed power's angle dependency in the magnetic material is denoted by $A \sin^2\theta + B$, while ISHE detection follows a $\cos\theta$ relationship. The contributions of these two parts to the voltage are depicted in Fig. 13.

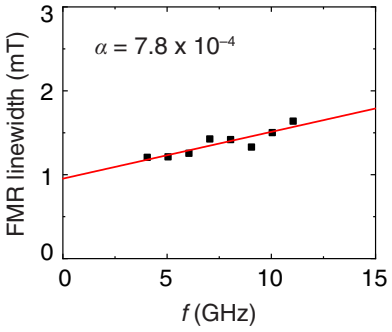

FIG. 10. The FMR properties of the YIG/Pt bilayer, with the points showing experimental data and the curves showing linear fitting.

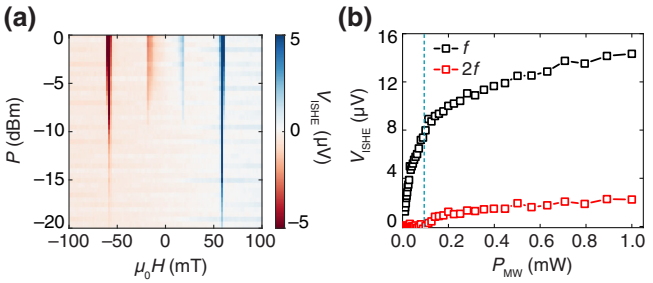

FIG. 12. (a) The power-dependent measurement with sweeping the external magnetic field from −100 to 100 mT, keeping the frequency fixed at 3 GHz. (b) The extracted voltage strengths of the main mode and parametric pumping mode as a function of power.

APPENDIX J: ANGLE-DEPENDENT PROPAGATION SPECTRA OF SPIN WAVES

To signify the involvement of propagating dipolar-exchange spin waves in contributing to the nonreciprocal nonlocal detection of ISHE voltage, the control measurement of the angle-dependent spin waves is also measured on the two NSL antennas with propagation distance $s =$ 2 μm. Figures 14(a) and 14(b) show angle-dependent spectra for S_{12} $(-k)$ and S_{21} $(+k)$, where a clear asymmetry is observed. This observation confirms the nonreciprocal nature of the V_{ISHE}, which is partially derived from the nonreciprocity of propagating dipolar-exchange spin waves.

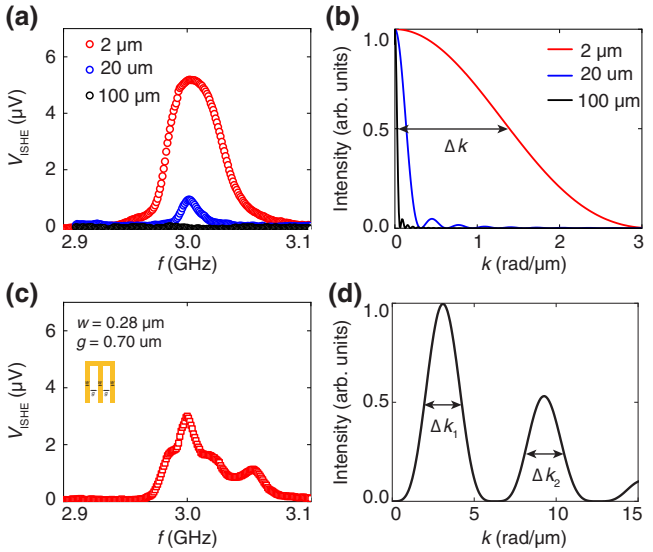

FIG. 11. (a) Frequency-dependent V_{ISHE} measured in devices with different widths of NSL at $\mu_0 H = 51$ mT and $P_{\mathrm{mW}} =$ 63 μW. (b) The broad-wave-vector distribution is calculated by varying the widths of NSL using FFT, and for NSL antennas of widths 2, 20, and 100 μm, the corresponding values of Δk are 1.5, 0.15, and 0.03 rad/μm respectively. (c) Frequency-dependent V_{ISHE} measured in CPW. The width of signal line and ground line is 0.28 μm, the gap between signal line and ground lines is 0.7 μm. The Fourier spectrum of the dynamic in-plane magnetic field distribution generated by the ground-signal-ground CPW is shown. (d) δk_1 and δk_2 are the effective excitation wave vector of CPW, both equal to 2.2 rad/μm.

APPENDIX K: ANGLE-DEPENDENT PUMPING SPECTRA UNDER HIGH-POWER EXCITATION

The current focus on nonlinear processes within the research community is noteworthy. Examining Fig. 12, it is evident that beyond 0.1 mW (−10 dBm), when the main mode enters the nonlinear regime, the strength of nonlinear modes, particularly parametric pumping, undergoes a rapid and significant enhancement. This observation underscores the substantial contribution of nonlinear processes under

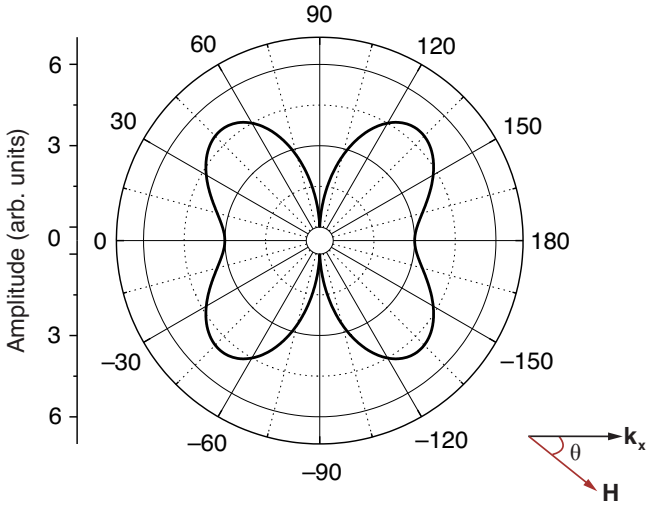

FIG. 13. ISHE's angular dependence multiplied by the angular dependency of power absorption, as computed by $\cos\theta(A \sin^2\theta + B)$.

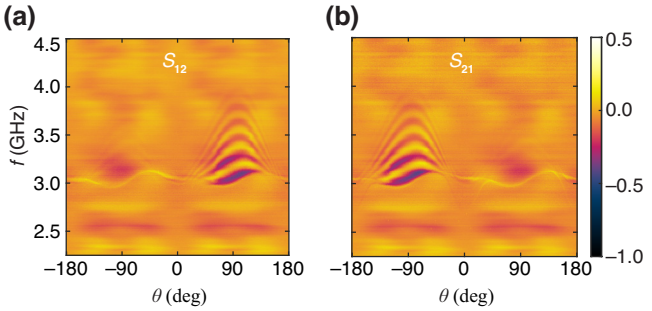

FIG. 14. The inductive coupling spin-wave propagation spectra S_{12} (a) and S_{21} (b) measured as a function of the angle θ. The field is fixed at 52 mT. θ is defined as the angle between **H** and k.

high-power excitation. This leads us to explore the angle-dependent pumping feature within the nonlinear regime. Specifically, we concentrate on the highest power (1.0 mW) highlighted in Fig. 2(b) in the main text, conducting angle-dependent spectra measurements for $+k$ magnons. The resulting spectra are illustrated in Fig. 15(a). To enable a thorough comparison with the spectra under low-power excitation, we extract the maximum voltage as a function of angle [Fig. 15(b)], facilitating a direct comparison with features observed in the linear regime, as presented in Fig. 3(b) in the main text. In the nonlinear regime, nonreciprocity is suppressed, potentially due to the significant population of magnons accumulating near the excitation antenna. This accumulation results in a more homogeneous profile of the surface mode along the thickness. Nevertheless, the broad flatband-enhanced pumping feature remains consistent with the linear scenario, where the maximum pumping voltages are situated within the flatband configuration range, specifically between 20 and 30°.

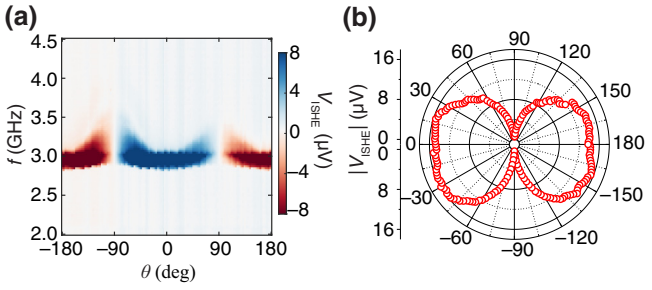

FIG. 15. (a) Angle-dependent spectra of V_{ISHE} for $+k$ magnons at $\mu_0 H = 52$ mT in nonlinear regime with $P_{MW} =$ 1 mW. (b) Angular dependence of the absolute voltage with the extraction of maximum V_{ISHE} values at each angle from $+k$ spectrum in (a).

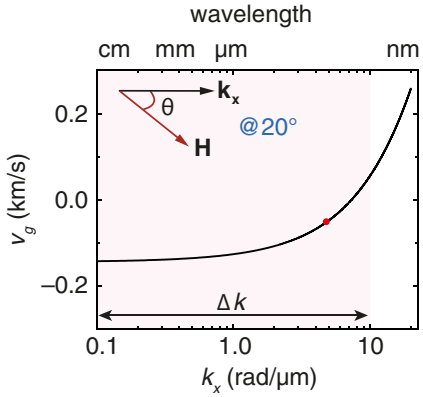

FIG. 16. The spin-wave group velocity as a function of wave vector at 20°. The red point is the corresponding wave-vector value 5.2 rad/μm with the experimentally estimated spin-wave group velocity 0.04 km/s in the distance-dependent measurement.

APPENDIX L: CALCULATED SPIN-WAVE GROUP VELOCITY AS A FUNCTION OF WAVE VECTOR AT 20°

Based on the extracted decay length from the distance-dependent measurement, we are able to experimentally estimate the spin-wave group velocity about 0.037–0.044 km/s. To compare this value with the dispersion curves in the main text, we use Eqs. (4) and (5) and $v_g = 2\pi \partial f / \partial k$ to calculate the spin-wave group velocity as a function of wave vector at 20° as shown in Fig. 16. When the wave vector is about 5.22–5.56 rad/μm located at the center of the broad range of the wave vector provided by the width of the antenna, the calculated group velocity matches with the experimentally estimated one (red point in Fig. 16).

[1] V. V. Kruglyak, S. O. Demokritov, and D. Grundler, Magnonics, J. Phys. D: Appl. Phys. **43**, 264001 (2010).
[2] Y. Fan, J. Finley, J. Han, M. E. Holtz, P. Quarterman, P. Zhang, T. S. Safi, J. T. Hou, A. J. Grutter, and L. Liu, Resonant spin transmission mediated by magnons in a magnetic insulator multilayer structure, Adv. Mater. **33**, 2008555 (2021).
[3] B. Lenk, H. Ulrichs, F. Garbs, and M. Münzenberg, The building blocks of magnonics, Phys. Rep. **507**, 107 (2011).
[4] A. V. Chumak, V. I. Vasyuchka, A. A. Serga, and B. Hillebrands, Magnon spintronics, Nat. Phys. **11**, 453 (2015).
[5] P. Pirro, V. I. Vasyuchka, A. A. Serga, and B. Hillebrands, Advances in coherent magnonics, Nat. Rev. Mater. **6**, 1114 (2021).
[6] H. Yu, J. Xiao, and H. Schultheiss, Magnetic texture based magnonics, Phys. Rep. **905**, 1 (2021).
[7] J. Chen, H. Yu, and G. Gubbiotti, Unidirectional spin-wave propagation and devices, J. Phys. D: Appl. Phys. **55**, 123001 (2022).

[8] A. A. Serga, A. V. Chumak, and B. Hillebrands, YIG magnonics, J. Phys. D: Appl. Phys. **43**, 264002 (2010).

[9] A. V. Chumak, A. A. Serga, and B. Hillebrands, Magnon transistor for all-magnon data processing, Nat. Commun. **5**, 4700 (2014).

[10] J. Chen, H. Wang, T. Hula, C. Liu, S. Liu, T. Liu, H. Jia, Q. Song, C. Guo, Y. Zhang, *et al.*, Reconfigurable spin-wave interferometer at the nanoscale, Nano Lett. **21**, 6237 (2021).

[11] J. Bass and W. P. Pratt, Spin-diffusion lengths in metals and alloys, and spin-flipping at metal/metal interfaces: an experimentalist's critical review, J. Phys. Condens. Matter **19**, 183201 (2007).

[12] R. Jansen, S. P. Dash, S. Sharma, and B. C. Min, Silicon spintronics with ferromagnetic tunnel devices, Semicond Sci. Technol. **27**, 083001 (2012).

[13] J. Han, R. Cheng, L. Liu, H. Ohno, and S. Fukami, Coherent antiferromagnetic spintronics, Nat. Mater. **22**, 684 (2023).

[14] K. Ganzhorn, S. Klingler, T. Wimmer, S. Geprägs, R. Gross, H. Huebl, and S. T. B. Goennenwein, Magnon-based logic in a multi-terminal YIG/Pt nanostructure, Appl. Phys. Lett. **109**, 022405 (2016).

[15] P. Monod, H. Hurdequint, A. Jánossy, J. Obert, and J. Chaumont, Giant electron spin-resonance transmission in Cu ion implanted with Mn, Phys. Rev. Lett. **29**, 1327 (1972).

[16] A. Jánossy and P. Monod, Spin waves for single electrons in paramagnetic metals, Phys. Rev. Lett. **37**, 612 (1976).

[17] Y. Tserkovnyak, A. Brataas, and G. E. W. Bauer, Spin pumping and magnetization dynamics in metallic multilayers, Phys. Rev. B **66**, 224403 (2002).

[18] Y. S. Chen, J. G. Lin, S. Y. Huang, and C. L. Chien, Incoherent spin pumping from YIG single crystals, Phys. Rev. B **99**, 220402(R) (2019).

[19] O. Mosendz, V. Vlaminck, J. E. Pearson, F. Y. Fradin, G. E. W. Bauer, S. D. Bader, and A. Hoffmann, Detection and quantification of inverse spin Hall effect from spin pumping in permalloy/normal metal bilayers, Phys. Rev. B **82**, 214403 (2010).

[20] D. Wei, M. Obstbaum, M. Ribow, C. H. Back, and G. Woltersdorf, Spin Hall voltages from a.c. and d.c. spin currents, Nat. Commun. **5**, 3768 (2014).

[21] K. Ando, Y. Kajiwara, S. Takahashi, S. Maekawa, K. Takemoto, M. Takatsu, and E. Saitoh, Angular dependence of inverse spin-Hall effect induced by spin pumping investigated in a $Ni_{81}Fe_{19}$/Pt thin film, Phys. Rev. B **78**, 014413 (2008).

[22] S. Gupta, R. Medwal, D. Kodama, K. Kondou, Y. Otani, and Y. Fukuma, Important role of magnetization precession angle measurement in inverse spin Hall effect induced by spin pumping, Appl. Phys. Lett. **110**, 022404 (2017).

[23] Y. Wang, M. M. Decker, T. N. G. Meier, X. Chen, C. Song, T. Grünbaum, W. Zhao, J. Zhang, L. Chen, and C. H. Back, Spin pumping during the antiferromagnetic–ferromagnetic phase transition of iron-rhodium, Nat. Commun. **11**, 275 (2020).

[24] H. Liu, H. Malissa, R. M. Stolley, J. Singh, M. Groesbeck, H. Popli, M. Kavand, S. K. Chong, V. V. Deshpande, J. S. Miller, *et al.*, Spin wave excitation, detection, and utilization in the organic-based magnet, $V(TCNE)_x$ (TCNE = Tetracyanoethylene), Adv. Mater. **32**, 2002663 (2020).

[25] Y. Kajiwara, K. Harii, S. Takahashi, J. Ohe, K. Uchida, M. Mizuguchi, H. Umezawa, H. Kawai, K. Ando, K. Takanashi, *et al.*, Transmission of electrical signals by spin-wave interconversion in a magnetic insulator, Nature **464**, 262 (2010).

[26] H. Wang, R. Yuan, Y. Zhou, Y. Zhang, J. Chen, S. Liu, H. Jia, D. Yu, J.-P. Ansermet, C. Song, and H. Yu, Long-distance coherent propagation of high-velocity antiferromagnetic spin waves, Phys. Rev. Lett. **130**, 096701 (2023).

[27] M. Hamdi, F. Posva, and D. Grundler, Spin wave dispersion of ultra-low damping hematite (α-Fe_2O_3) at GHz frequencies, Phys. Rev. Mater. **7**, 054407 (2023).

[28] A. El Kanj, O. Gomonay, I. Boventer, P. Bortolotti, V. Cros, A. Anane, and R. Lebrun, Antiferromagnetic magnon spintronic based on nonreciprocal and nondegenerated ultra-fast spin-waves in the canted antiferromagnet α-Fe_2O_3, Sci. Adv. **9**, eadh1601 (2023).

[29] M. Haertinger, C. H. Back, J. Lotze, M. Weiler, S. Geprägs, H. Huebl, S. T. B. Goennenwein, and G. Woltersdorf, Spin pumping in YIG/Pt bilayers as a function of layer thickness Phys. Rev. B **92**, 054437 (2015).

[30] V. Castel, N. Vlietstra, B. J. van Wees, and J. B. Youssef, Frequency and power dependence of spin-current emission by spin pumping in a thin-film YIG/Pt system, Phys. Rev. B **86**, 134419 (2012).

[31] M. B. Jungfleisch, A. V. Chumak, A. Kehlberger, V. Lauer, D. H. Kim, M. C. Onbasli, C. A. Ross, M. Kläui, and B. Hillebrands, Thickness and power dependence of the spin-pumping effect in $Y_3Fe_5O_{12}$/Pt heterostructures measured by the inverse spin Hall effect, Phys. Rev. B **91**, 134407 (2015).

[32] H. L. Wang, C. H. Du, Y. Pu, R. Adur, P. C. Hammel, and F. Y. Yang, Large spin pumping from epitaxial $Y_3Fe_5O_{12}$ thin films to Pt and W layers, Phys. Rev. B **88**, 100406(R) (2013).

[33] S. Takizawa, M. Kimata, Y. Omori, Y. Niimi, and Y. Otani, Spin mixing conductance in Cu–Ir dilute alloys, Appl. Phys. Express **9**, 063009 (2016).

[34] M. Weiler, M. Althammer, M. Schreier, J. Lotze, M. Pernpeintner, S. Meyer, H. Huebl, R. Gross, A. Kamra, J. Xiao, *et al.*, Experimental test of the spin mixing interface conductivity concept, Phys. Rev. Lett. **111**, 176601 (2013).

[35] S. Maekawa, S. O. Valenzuela, E. Saitoh, and T. Kimura, *Spin Current* (Oxford University Press, Oxford, 2017), Vol. 22.

[36] S. Maekawa, T. Kikkawa, H. Chudo, J. Ieda, and E. Saitoh, Spin and spin current–from fundamentals to recent progress, J. Appl. Phys. **133**, 020902 (2023).

[37] O. Mosendz, J. E. Pearson, F. Y. Fradin, G. E. W. Bauer, S. D. Bader, and A. Hoffmann, Quantifying spin Hall angles from spin pumping: Experiments and theory, Phys. Rev. Lett. **104**, 046601 (2010).

[38] Y. Sun, H. Chang, M. Kabatek, Y.-Y. Song, Z. Wang, M. Jantz, W. Schneider, M. Wu, E. Montoya, B. Kardasz, *et al.*, Damping in yttrium iron garnet nanoscale films capped by platinum, Phys. Rev. Lett. **111**, 106601 (2013).

[39] M. V. Costache, M. Sladkov, S. M. Watts, C. H. van der Wal, and B. J. van Wees, Electrical detection of spin pumping due to the precessing magnetization of a single ferromagnet, Phys. Rev. Lett. **97**, 216603 (2006).

[40] K. Ando, J. Ieda, K. Sasage, S. Takahashi, S. Maekawa, and E. Saitoh, Electric detection of spin wave resonance using inverse spin-Hall effect, Appl. Phys. Lett. **94**, 262505 (2009).

[41] P. Wang, Spin pumping by higher-order dipole-exchange spin-wave modes, Chin. Phys. B **32**, 037601 (2023).

[42] A. V. Chumak, A. A. Serga, M. B. Jungfleisch, R. Neb, D. A. Bozhko, V. S. Tiberkevich, and B. Hillebrands, Direct detection of magnon spin transport by the inverse spin Hall effect, Appl. Phys. Lett. **100**, 082405 (2012).

[43] S. S. Mukherjee, P. Deorani, J. H. Kwon, and H. Yang, Attenuation characteristics of spin-pumping signal due to traveling spin waves, Phys. Rev. B **85**, 094416 (2012).

[44] C. W. Sandweg, Y. Kajiwara, K. Ando, E. Saitoh, and B. Hillebrands, Enhancement of the spin pumping efficiency by spin wave mode selection, Appl. Phys. Lett. **97**, 252504 (2010).

[45] S. Dushenko, Y. Higuchi, Y. Ando, T. Shinjo, and M. Shiraishi, Ferromagnetic resonance and spin pumping efficiency for inverse spin-Hall effect normalization in yttrium-iron-garnet-based systems, Appl. Phys. Express **8**, 103002 (2015).

[46] R. Iguchi, K. Ando, Z. Qiu, T. An, E. Saitoh, and T. Sato, Spin pumping by nonreciprocal spin waves under local excitation, Appl. Phys. Lett. **102**, 022406 (2013).

[47] T. Bracher, M. Fabre, T. Meyer, T. Fischer, S. Auffret, O. Boulle, U. Ebels, P. Pirro, and G. Gaudin, Detection of short-waved spin waves in individual microscopic spin-wave waveguides using the inverse spin Hall effect, Nano Lett. **17**, 7234 (2017).

[48] S. A. Manuilov, C. H. Du, R. Adur, H. L. Wang, V. P. Bhallamudi, F. Y. Yang, and P. C. Hammel, Spin pumping from spinwaves in thin film YIG, Appl. Phys. Lett. **107**, 042405 (2015).

[49] M. Fukami, Y. Tateno, K. Sekiguchi, and K. Ando, Wave-vector-dependent spin pumping as a probe of exchange-coupled magnons, Phys. Rev. B **93**, 184429 (2016).

[50] K. Ando and E. Saitoh, Spin pumping driven by bistable exchange spin waves, Phys. Rev. Lett. **109**, 026602 (2012).

[51] C. W. Sandweg, Y. Kajiwara, A. V. Chumak, A. A. Serga, V. I. Vasyuchka, M. B. Jungfleisch, E. Saitoh, and B. Hillebrands, Spin pumping by parametrically excited exchange magnons, Phys. Rev. Lett. **106**, 216601 (2011).

[52] H. Kurebayashi, O. Dzyapko, V. E. Demidov, D. Fang, A. J. Ferguson, and S. O. Demokritov, Spin pumping by parametrically excited short-wavelength spin waves, Appl. Phys. Lett. **99**, 162502 (2011).

[53] G. Csaba, Á. Papp, and W. Porod, Perspectives of using spin waves for computing and signal processing, Phys. Lett. A **381**, 1471 (2017).

[54] T. Liu, H. Chang, V. Vlaminck, Y. Sun, M. Kabatek, A. Hoffmann, L. Deng, and M. Wu, Ferromagnetic resonance of sputtered yttrium iron garnet nanometer films, J. Appl. Phys. **115**, 17A501 (2014).

[55] O. d'Allivy Kelly, A. Anane, R. Bernard, J. Ben Youssef, C. Hahn, A. H. Molpeceres, C. Carrétéro, E. Jacquet, C. Deranlot, P. Bortolotti, *et al.*, Inverse spin Hall effect in nanometer-thick yttrium iron garnet/Pt system, Appl. Phys. Lett. **103**, 082408 (2013).

[56] Y. Sun, Y.-Y. Song, H. Chang, M. Kabatek, M. Jantz, W. Schneider, M. Wu, H. Schultheiss, and A. Hoffmann, Growth and ferromagnetic resonance properties of nanometer-thick yttrium iron garnet films, Appl. Phys. Lett. **101**, 152405 (2012).

[57] B. A. Kalinikos and A. N. Slavin, Theory of dipole-exchange spin wave spectrum for ferromagnetic films with mixed exchange boundary conditions, J. Phys. C: Solid State Phys. **19**, 7013 (1986).

[58] R. A. Gallardo, D. Cortés-Ortuno, T. Schneider, A. Roldán-Molina, F. Ma, R. E. Troncoso, K. Lenz, H. Fangohr, J. Lindner, and P. Landeros, Flat bands, indirect gaps, and unconventional spin-wave behavior induced by a periodic Dzyaloshinskii-Moriya interaction, Phys. Rev. Lett. **122**, 067204 (2019).

[59] J. Chen, L. Zeng, H. Wang, M. Madami, G. Gubbiotti, S. Liu, J. Zhang, Z. Wang, W. Jiang, Y. Zhang, *et al.*, Magic-angle magnonic nanocavity in a magnetic moiré superlattice, Phys. Rev. B **105**, 094445 (2022).

[60] H. Wang, M. Madami, J. Chen, H. Jia, Y. Zhang, R. Yuan, Y. Wang, W. He, L. Sheng, Y. Zhang, *et al.*, Observation of spin-wave moiré edge and cavity modes in twisted magnetic lattices, Phys. Rev. X **13**, 021016 (2023).

[61] S. Tacchi, J. Flores-Farías, D. Petti, F. Brevis, A. Cattoni, G. Scaramuzzi, D. Girardi, D. Cortés-Ortuño, R. A. Gallardo, E. Albisetti, *et al.*, Experimental observation of flat bands in one-dimensional chiral magnonic crystals, Nano Lett. **23**, 6776 (2023).

[62] M. Althammer, Pure spin currents in magnetically ordered insulator/normal metal heterostructures, J. Phys. D: Appl. Phys. **51**, 313001 (2018).

[63] F. Yang and P. C. Hammel, FMR-driven spin pumping in $Y_3Fe_5O_{12}$-based structures, J. Phys. D: Appl. Phys. **51**, 253001 (2018).

[64] T. Holstein and H. L. Primakoff, Field dependence of the intrinsic domain magnetization of a ferromagnet, Phys. Rev. **58**, 1098 (1940).

[65] H. L. Wang, C. H. Du, Y. Pu, R. Adur, P. C. Hammel, and F. Y. Yang, Scaling of spin Hall angle in 3*d*, 4*d*, and 5*d* metals from $Y_3Fe_5O_{12}$/metal spin pumping, Phys. Rev. Lett. **112**, 197201 (2014).

[66] F. D. Czeschka, L. Dreher, M. S. Brandt, M. Weiler, M. Althammer, I.-M. Imort, G. Reiss, A. Thomas, W. Schoch, and W. Limmer, Scaling behavior of the spin pumping effect in ferromagnet-platinum bilayers, Phys. Rev. Lett. **107**, 046601 (2011).

[67] E. Shikoh, K. Ando, K. Kubo, E. Saitoh, T. Shinjo, and M. Shiraishi, Spin-pump-induced spin transport in p-type Si at room temperature, Phys. Rev. Lett. **110**, 127201 (2013).

[68] M. Harder, Y. Gui, and C.-M. Hu, Electrical detection of magnetization dynamics via spin rectification effects, Phys. Rep. **661**, 1 (2016).

[69] K. He, J. Cheng, M. Yang, Y. Zhang, L. Yu, Q. Liu, L. Sun, B. Miao, C. Hu, and H. Ding, Spin rectification effect induced by planar Hall effect and its strong impact on spin-pumping measurements, Phys. Rev. B **105**, 104406 (2022).

[70] K-I. Uchida, S. Takahashi, K. Harii, J. Ieda, W. Koshibae, K. Ando, S. Maekawa, and E. Saitoh, Observation of the spin Seebeck effect, Nature **455**, 778 (2008).

[71] H. Yu, O. d'Allivy Kelly, V. Cros, R. Bernard, P. Bortolotti, A. Anane, F. Brandl, R. Huber, I. Stasinopoulos, and D. Grundler, Magnetic thin-film insulator with ultra-low spin wave damping for coherent nanomagnonics, Sci. Rep. **4**, 6848 (2014).

[72] H. Wang, W. He, R. Yuan, Y. Wang, J. Wang, Y. Zhang, I. Medlej, J. Chen, G. Yu, X. Han, *et al.*, Hybridized propagating spin waves in a CoFeB/IrMn bilayer, Phys. Rev. B **106**, 064410 (2022).

[73] J. Chen, T. Yu, C. Liu, T. Liu, M. Madami, K. Shen, J. Zhang, S. Tu, M. S. Alam, K. Xia, *et al.*, Excitation of unidirectional exchange spin waves by a nanoscale magnetic grating, Phys. Rev. B **100**, 104427 (2019).

[74] A. Prabhakar and D. D. Stancil, *Spin Waves: Theory and Applications* (Springer, Boston, MA, 2009), Vol. 5.

[75] A. A. Serga, A. V. Chumak, A. André, G. A. Melkov, A. N. Slavin, S. O. Demokritov, and B. Hillebrands, Parametrically stimulated recovery of a microwave signal stored in standing spin-wave modes of a magnetic film, Phys. Rev. Lett. **99**, 227202 (2007).

[76] L. Sheng, M. Elyasi, J. Chen, W. He, Y. Wang, H. Wang, H. Feng, Y. Zhang, I. Medlej, S. Liu, *et al.*, Nonlocal detection of interlayer three-magnon coupling, Phys. Rev. Lett. **130**, 046701 (2023).

[77] K. Ando, S. Takahashi, J. Ieda, Y. Kajiwara, H. Nakayama, T. Yoshino, K. Harii, Y. Fujikawa, M. Matsuo, S. Maekawa, *et al.*, Inverse spin-Hall effect induced by spin pumping in metallic system, J. Appl. Phys. **109**, 103913 (2011).

[78] H. Qin, S. J. Hämäläinen, K. Arjas, J. Witteveen, and S. Van Dijken, Propagating spin waves in nanometer-thick yttrium iron garnet films: Dependence on wave vector, magnetic field strength, and angle, Phys. Rev. B **98**, 224422 (2018).

[79] A. Talalaevskij, M. Decker, J. Stigloher, A. Mitra, H. S. Körner, O. Cespedes, C. H. Back, and B. J. Hickey, Magnetic properties of spin waves in thin yttrium iron garnet films, Phys. Rev. B **95**, 064409 (2017).

[80] X.-Y. Wei, O. Alves Santos, C. H. Sumba Lusero, G. E. W. Bauer, J. Ben Youssef, and B. J. van Wees, Giant magnon spin conductivity in ultrathin yttrium iron garnet films, Nat. Mater. **21**, 1352 (2022).

[81] H. Yu, R. Huber, T. Schwarze, F. Brandl, T. Rapp, P. Berberich, G. Duerr, and D. Grundler, High propagating velocity of spin waves and temperature dependent damping in a CoFeB thin film, Appl. Phys. Lett. **100**, 262412 (2012).

[82] H. Nakayama, M. Althammer, Y. T. Chen, K. Uchida, Y. Kajiwara, D. Kikuchi, T. Ohtani, S. Geprägs, M. Opel, S. Takahashi, R. Gross, G. E. W. Bauer, S. T. B. Goennenwein, and E. Saitoh, Spin Hall magnetoresistance induced by a nonequilibrium proximity effect, Phys. Rev. Lett. **110**, 206601 (2013).

[83] J. D. Jackson, *Classical Electrodynamics* (Wiley, New York, 1999), 3rd ed.